Performance enhancement of underwater propulsion motor using differential evolution optimization

M. Rezal[1] & Dahaman Ishak[2*]

[1]Universiti Kuala Lumpur, Malaysian Spanish Institute, Kulim Hi-Tech Park, 09000 Kulim, Kedah, Malaysia

[2]School of Electrical & Electronic Engineering, Universiti Sains Malaysia, 14300 Nibong Tebal, Penang, Malaysia

*[E-mail: dahaman@usm.my]

This paper describes the performance enhancement of underwater propulsion motor using differential evolution optimization (DEO). Usually during development stage, an analytical subdomain model (ASM) is often preferred to be used in the design of electric machines since ASM has faster computational time compared to the finite element method. differential evolution algorithm is deployed to provide the optimization process in searching the optimal motor parameters iteratively and intelligently with specific objective functions. For this purpose, a three-phase, 6-slot/4-pole permanent magnet synchronous motor (PMSM) intended for the underwater propulsion system is first designed by using ASM and then later optimized by differential evolution algorithm. Five main motor parameters, i.e., magnet pole arc, magnet thickness, air gap length, slot opening, and stator inner radius are varied and optimized to achieve the design objective functions, i.e., high motor efficiency, high output torque, low total harmonic distortion (THDv) in back-emf, and low cogging torque. Results from differential evolution optimization show an improved performance of the proposed PMSM where the efficiency of the motor is increased to 96.1% from its initial value of 94.2%, 13% increase in the output torque, and 4.1% reduction for total harmonic distortion in its back-emf. Therefore, DEO can be highly considered during initial design stage to optimize the motor parameters in developing a good underwater propulsion motor.

[**Keywords**: Underwater propulsion motor; Analytical subdomain; Differential evolution]

Introduction

The use of electrical motor and power electronic converter for the electric propulsion systems in the underwater robotics and underwater vehicles is gaining popularity due to their compactness, light weight and control simplicity. Induction motor, DC motor, switched reluctance motor, and permanent magnet synchronous motor are several types of electrical motors that can be used for the underwater propulsion systems. For instance, a three-phase induction motor for underwater propulsion systems reported[1]. Not only that, separately excited DC motor can also be used by varying its duty cycle using closed-loop control of chopper fed DC drive[2]. Switched reluctance motor with new buck-boost converter able to have high demagnetization voltage using hysteresis current controller was tested for underwater propulsion motor[3]. A model identification and control analysis for brushless DC motor using four-type system identifications was applied for underwater thruster system[4]. A DC brushed electric thruster was developed using statistical design of experiment by applying two factorial designs, i.e.,

armature voltage and thruster condition[5]. Performance comparison of electric underwater thruster was conducted using computational fluid dynamic model and experimental measurement[6]. There is a linear relationship between speed, thrust and power of the thruster. Increasing the thruster speed will increase the thrust and power of the thruster and vice versa. A small-scale electrically actuated thruster was developed which shows a good performance for the autonomous underwater vehicle application[7]. However, permanent magnet synchronous machines for the underwater propulsion motor due to their high efficiency, high torque density and good dynamic performance[8]. Rotor magnetic flux is readily available and continuously generated without consumption of input energy by placing permanent magnet materials in the rotor core. Hence, rotor loss is significantly reduced because the rotor does not carry the field winding and magnetizing current. PMSM can be classified by the manner the permanent magnet materials are placed in the rotor core, such as surface-mounted magnet, surface-inset magnet, bread loaf magnet, interior magnet, and spoke magnet[9]. Surface-mounted type of

PMSM can utilize the most magnetic flux compared with other types since the magnet materials are placed next to the air gap, and hence magnetic leakage is almost negligible[10]. The structure of the stator can be either slotted or slotless. Slotless structure has advantages over slotted structure as the slotless structures eliminate cogging torque, exhibit low armature reaction and low inductance due to higher effective air-gap length[11,12]. There are possibly five different magnetization patterns that can be applied for surface-mounted PMSM: Radial magnetization, parallel magnetization, sinusoidal amplitude magnetization, ideal Halbach, and multi-segmented Halbach. Each of these magnetization patterns can be represented in 2D polar coordinate system in the radial and tangential directions as reported in[13,14]. In an earlier study[7], the authors only studied the motor performance using radial magnetization of permanent magnet and the motor dimensions were not fully optimized. There are many optimization models that can be used to identify the optimal motor parameters namely, genetic algorithm, particle swarm optimization, or differential evolution. In this paper, the performance of a three-phase, 6-slot/4-pole PMSM is investigated before and after optimization using analytical subdo main model integrated with differential evolution algorithm. This motor employs fractional slot concentrated windings, slotted stator and surface-mounted permanent magnet rotor. The computed results from the optimization exercise are further analysed and compared with 2D finite element method (FEM).

Motor Design Parameters

The dimensions of the three-phase, 6-slot/4-pole PMSM are shown in Table 1. The permanent magnet mounted on the rotor surface is initially fixed to have 3 mm thickness. The stator outside diameter is 50 mm, while the axial length is 100 mm. The phase windings and magnet arrangement in the 6-slot/4-pole motor are shown in Figure 1. The stator coils and coil emf vectors in the 6-slot/4-pole are shown in Figure 2. It has symmetric windings since phase A windings are wound on stator teeth number 1 and 4, resulting in balanced magnetic pulls. The magnitude of the coil back-emf is influenced by the pitch-factor K_{pn}. The derivation of K_{pn} given in Eq. (1)[15], where N_s is the number of stator slots, p is the number of pole pairs, and n is the harmonics numbers. The distribution factor K_{dn} is given by

Eq. (2) which is unity for the case of this 6-slot/4-pole PMSM. Hence, the winding factor K_{dpn} is shown in Eq. (3). The open-circuit flux-linkage per coil, ψ_{coil} of the motor can be estimated by Eq. (4), where R_s, l_a, N_c, B_n and ω_r are the stator inner radius, motor active axial length, number of turns per coil, magnitude of flux density, and rotor angular speed in rad/s[15].

$$K_{pn} = \cos(np\pi/N_s) \qquad \text{… (1)}$$

$$K_{dn} = 1 \qquad \text{… (2)}$$

$$K_{dpn} = \cos(np\pi/N_s) \qquad \text{… (3)}$$

$$\psi_{coil} = 2R_s l_a N_c \sum_{n=1,3,5\ldots}^{\infty} K_{pn} B_n(R_s) \cos(np\omega_r t) \qquad \text{… (4)}$$

Table 1 — Dimensions of three-phase, 6-slot/4-pole PMSM

| Parameters	Value
Stator outer radius, mm	25.0
Stator yoke thickness, mm	3.4
Tooth body, mm	6.8
Tooth tip height, mm	2.3
Tooth end, mm	1.5
Stator slot opening, mm	2.0
Stator inner radius, mm	15.0
Magnet outer radius, mm	14.0
Rotor outer radius, mm	11.0
Radial rotor yoke, mm	5.0
Active axial length, mm	100.0
Magnet remanence, T	1.26
Winding turns per phase	50
Rated speed, rpm	1500
Rated torque, Nm	0.9
Magnet pole arc	0.8
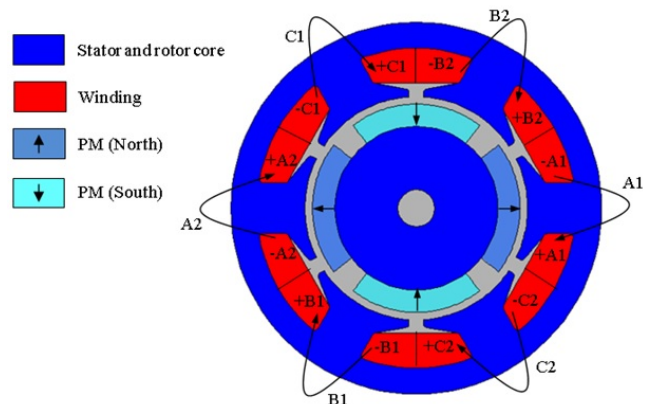
Fig. 1 — Allocation of phase windings and magnets arrangement for 6-slot/4-pole PMSM

(a) Stator coils of 6-slot/4-pole in mechanical degree   (b) emf vectors of 6-slot/4-pole
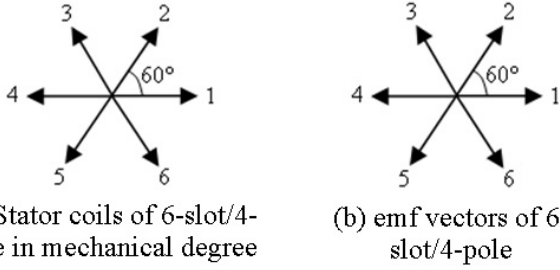
Fig. 2 —Stator coils and coil emf vectors for 6-slot/4-pole PMSM

Analytical Sub-Domain Modelling

Analytical subdomain model (ASM) utilizes separation of variables technique to derive the general field solutions of Laplace's equation are derived for the air gap and slot opening regions; while, the field solutions of the quasi-Poisson's equation for the magnet and winding slot regions[16,17]. The magnetic field distributions, induced back-emf, electromagnetic torque, and cogging torque can be determined from ASM[18,19]. The air-gap magnetic flux densities can be determined using Eqs (5) and (6) for the radial and tangential components, respectively. The phase back-emf is defined as the rate of change of phase flux-linkage and is expressed in Eq. (7), where N_p is the number of series-connected winding turns per phase. Cogging torque is normally generated due to the interaction of rotor magnets with the stator slot openings. The cogging torque is predicted using Eq. (8)[20]. A Maxwell stress tensor is applied to determine this cogging torque, where l_a is the stack length, r is the air gap radius, μ_0 is the vacuum permeability, θ is the rotor angular position in electrical degree, while B_{srI} and $B_{s\theta I}$ are the radial and tangential components for slotted air-gap flux density. The efficiency of the PMSM is based on ratio of output power to the input power as shown in Eq. (9), where E_k is the rms phase voltage, I_k is the rms phase current, and R_{ph} is the phase resistance. For simplicity, the motor core loss and windage loss are first assumed to be negligible in estimating the motor efficiency. Most often, the dominant factor that affects motor efficiency is the copper loss.

$$B_{rI}(r,\theta) =$$
$$\sum_{n=1,3,5\ldots}^{\infty} \frac{\mu_o M_n}{2\mu_r} \cdot \frac{np}{(np)^2-1} \cdot \left(\frac{2\left[\left(\frac{R_r}{R_r}\right)^{np+1}-\left(\frac{R_r}{R_m}\right)^{2np}\right]}{\frac{\mu_r+1}{\mu_r}\left[1-\left(\frac{R_r}{R_s}\right)^{2np}\right]-\frac{\mu_r-1}{\mu_r}\left[\left(\frac{R_m}{R_s}\right)^{2np}-\left(\frac{R_r}{R_m}\right)^{2n}\right]} \right) \cdot$$
$$rRsnp-1RmRsnp+1+Rmrnp+1\cdot\cos np\theta \qquad \ldots (5)$$

$$B_{\theta I}(r,\theta) =$$
$$\sum_{n=1,3,5\ldots}^{\infty} \frac{\mu_o M_n}{2\mu_r} \cdot \frac{np}{(np)^2-1} \cdot \left(\frac{2\left[\left(\frac{R_r}{R_m}\right)^{np+1}-\left(\frac{R_r}{R_m}\right)^{2np}\right]}{\frac{\mu_r+1}{\mu_r}\left[1-\left(\frac{R_r}{R_s}\right)^{2np}\right]-\frac{\mu_r-1}{\mu_r}\left[\left(\frac{R_m}{R_s}\right)^{2np}-\left(\frac{R_r}{R_m}\right)^{2np}\right]} \right) \cdot$$
$$-rRsnp-1RmRsnp+1+Rmrnp+1\cdot\sin np\theta \qquad \ldots (6)$$

$$E_\emptyset = 2R_s N_p l_a \omega_r \sum_{n=1,3,5\ldots}^{\infty} K_{dpn} B_n(R_s) \sin(np\omega_r t) \qquad \ldots (7)$$

$$T_{cog}(r,\theta) = \frac{l_a}{\mu_0} \cdot r^2 \int_0^{2\pi} B_{srI(r,\theta)} \cdot B_{s\theta I(r,\theta)} d\theta \qquad \ldots (8)$$

$$\eta = \frac{\sum_{k=1}^{n=3} E_k I_k}{\sum_{k=1}^{n=3} E_k I_k + \sum_{k=1}^{n=3} I_k^2 R_{ph}} \cdot 100\% \qquad \ldots (9)$$

Optimization Technique

Differential evolution (DE) is one of the artificial intelligent algorithms that has originated from the genetic algorithm family. DE has four design processes, namely, population, mutation, crossover, and selection[21]. Therefore, DE is a population-based optimization method. A random population of Np D-dimensions with real-valued parameter vectors is generated. A candidate solution to the multi-dimensional optimization problem is formed from each vector, also known as genome/chromosome. The population at the current generation with each parameter of the ith vector has minimum and maximum bounds which can be represented in Eq. (10)[22]. A donor vector $W_{i,j}$ corresponding to each population member $Y_{i,j}$ in the current generation through mutation is generated. A mutation strategy as shown in Eq. (11) is applied, where F is a constant parameter called mutation scale factor[22]. A crossover operation is run after generating the donor vector through mutation to enhance the potential diversity of the population. The common binomial crossover is applied on each D variable whenever a randomly generated number between 0 and 1 is less than or equal to the crossover constant C_r value as shown in Eq. (12)[22]. To determine whether the target or the trial vector survives to the next generation, the selection step is applied. The selection operation is shown in Eq. (13)[22].

$$\vec{Y}_{i,j} = [y_{1,j}, y_{2,j}, y_{3,j}, \ldots, y_{D,j}] , \vec{y} \in R^D \qquad \ldots (10)$$

$$\vec{W}_{i,j} = \vec{Y}_{ro,j} + F \cdot (Y_{r1,j} - \vec{Y}_{r2,j}) \qquad \ldots (11)$$

$$\vec{U}_{i,j} = u_{k,i,j} = \begin{cases} w_{k,i,j} \; if \; r_k \leq C_r \; or \; k = k_{rand} \\ y_{k,i,j} \; if \; r_k > C_r \end{cases} \quad k = 1..n \quad \ldots (12)$$

$$\vec{y}_{i,j+1} = \begin{cases} \vec{U}_{i,j} \; if \; f(\vec{U}_{i,j}) \leq f(\vec{Y}_{i,j}) \\ \vec{Y}_{i,j} \; if \; f(\vec{U}_{i,j}) > f(\vec{Y}_{i,j}) \end{cases} \qquad \ldots (13)$$

Objective Functions

In this paper, four objective functions are selected, i.e., to have the lowest cogging torque, F_1; to have the lowest phase back-emf total harmonics distortion, F_2; to have the highest electromagnetic torque, F_3; and to

have the highest efficiency, F_4. The optimization results will be in vector form for each objective function and can be simplified as indicated in Eq. (14). The Pareto-chart is applied to identify the best motor parameters that give the best motor performances.

$$\mathcal{F}_{obj} = [\mathcal{F}_1, \mathcal{F}_2, \mathcal{F}_3', \mathcal{F}_4']_{min} \qquad \dots (14)$$

Optimized Parameters

Since the magnetic flux in the air gap region plays an important role in the PMSM performance, then five parameters near the air gap region will be optimized, i.e., magnet pole arc, α; magnet thickness, h_m; air gap length, l_g; slot opening, b_o; and stator inner radius, R_{si}, with certain constraints as listed in Table 2.

Results and Discussion
Pareto chart

To identify the best motor parameters, two Pareto charts are constructed to tabulate the four objective functions as shown in Figs 3 and 4. ASDEO is the acronym for analytical subdomain model integrated with differential evolution optimization. Output torque-initial means the motor output torque from the initial motor parameters as given in Table 1. As can be observed, the best motor performances are available in the square dotted line. After the best motor performance is selected, then the best motor parameters are applied for the optimized design of 6-slot/4-pole PMSM. Then, it is further verified using

FEM to validate its performances. Finally, the selected motor parameters that give the best motor performance is selected as given in Table 3.

As given in Table 3, the output torque has increased from 0.822 Nm to 0.928 Nm. The efficiency has improved by 1.9%, and THDv of phase back-emf has reduced by 4.1%. Whereas, the cogging torque remains unchanged. The magnet pole arc slightly increases from 0.8 to 0.9, but the air gap length is reduced by 10%. The slot opening is now 5% smaller, and stator inner radius has increased by 1 mm. Even though the magnet arc has increased which may affect the material cost, the motor efficiency and THDv of phase back-emf have been improved. The cogging torque is nearly 0.1 Nm which is as expected for this type of motor, but it can be further minimized by applying the cogging torque reduction techniques[23,25].

Finite element modelling

In this section, 2D FEM is used to compute the open-circuit air gap flux density distributions, the induced phase back-emf, cogging torque, and output torque for 6-slot/4-pole PMSM. The motor model with mechanical dimensions from Table 1 has been built in

Table 3 — Optimized 6-slot/4-pole motor dimensions and performances

Parameters	Initial	ASDEO
Magnet pole arc	0.8	0.9
Magnet thickness, mm	3.0	3.0
Air gap length, mm	1.0	0.9
Slot opening, mm	2.0	1.9
Stator inner radius, mm	15.0	16.0
Output torque, Nm	0.822	0.928
Efficiency, %	94.2	96.3
Phase back-emf THDv, %	8.32	4.2
Cogging torque, Nm	0.1	0.1

Table 2 — Parameter constraints

Values	Parameters				
	α	h_m, mm	l_g, mm	b_o, mm	R_{si}, mm
Maximum	1.0	3.0	1.0	2.0	18.0
Minimum	0.5	2.0	0.5	1.8	8.0
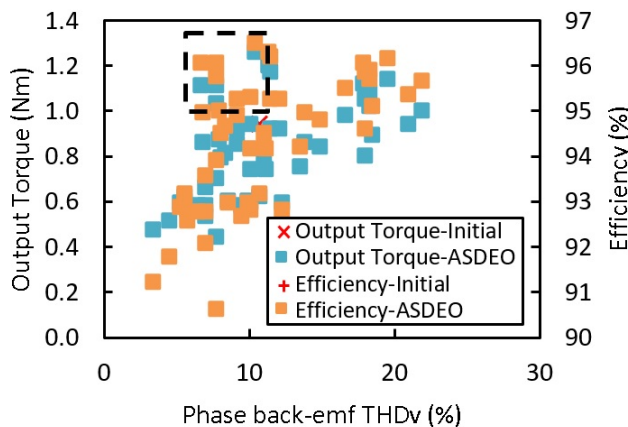
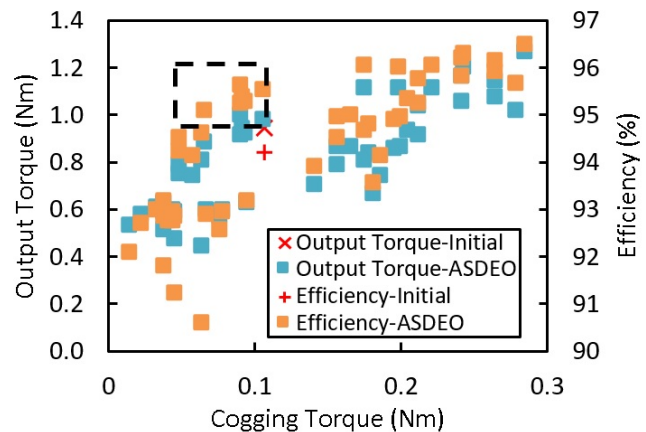Fig. 3 — THDv of phase back-emf versus output torque and efficiency

Fig. 4 — Cogging torque versus output torque and efficiency

2D finite element commercial software, i.e., OPERA2D. The stator and rotor core use silicon steel lamination. The magnet materials used are neodymium iron boron (NdFeB). The open-circuit magnetic flux density contour across motor sectional area can be plotted by applying static analysis in 2D FEM as shown in Figure 5. The motors are modelled with parallel magnetization patterns (PaM) in the rotor magnets. The open-circuit magnetic fields are balanced and equally distributed in the stator core of 6-slot/4-pole PMSM as indicated in Figure 5, yielding zero unbalanced magnetic force acting on the rotor. After being optimized, the maximum magnetic flux density that enters the motor core is reduced to 1.52 T, and this can prevent the core from extreme saturation during load conditions. The winding slot becomes smaller due to increase in stator yoke and tooth body of the motor. This is not a big problem since the total number of winding turns per phase is only 50
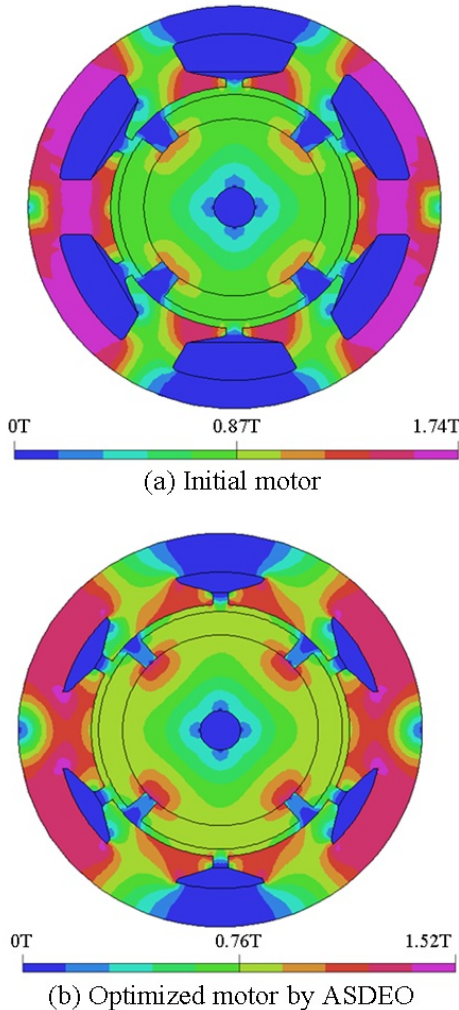
using 17 AWG copper wires. By using 2D FEM, the flux density distributions in the middle of the motor air gap can also be predicted as shown in Figure 6. There is not much difference in air gap magnetic flux density before and after optimization.

Phase back-emf waveform

The phase back-emf, electromagnetic torque and cogging torque for 6-slot/4-pole motor with PaM are evaluated by using 2D FEM. The peak voltage of phase back-emf increases to 20 V after it has been optimized
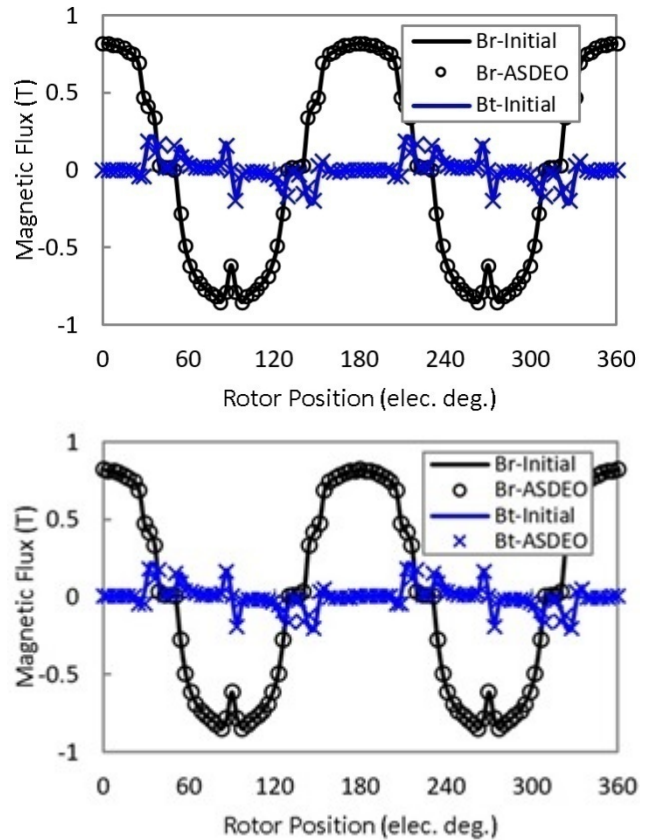

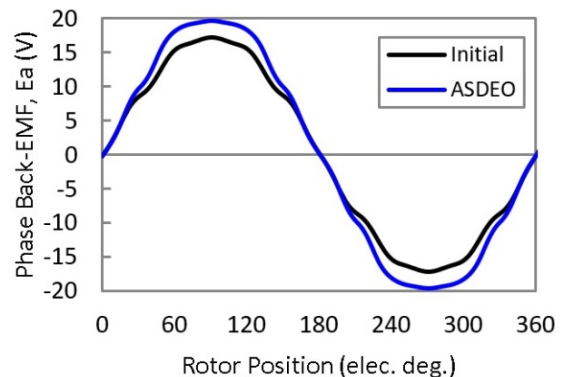Fig. 6 — Flux density distributions in the middle of air gap

(a) Initial motor

(b) Optimized motor by ASDEO

Fig. 5 — Open-circuit magnetic flux density contour for 6-slot/4-pole PMSM

Fig. 7 — Phase back-emf waveforms

Table 4 — Harmonic components in phase back-emf for 6-slot/4-pole motor

	THD$_v$ (%)	Magnitude of EMF Harmonics (V)			
		Fund.	5rd	7th	11th
Initial Motor	8.32	19.72	0.76	0.81	0.07
Motor after ASDEO	4.20	23.33	0.46	0.32	0.20

Table 5 — Output Torque

Parameters	Initial motor	Motor after ASDEO
Average EM Torque (Nm)	0.8215	0.9275
Peak-to-peak Torque Ripple (Nm)	0.2184	0.2101

Fig. 8 — Cogging torque waveforms

Fig. 9 — Output torque for 6-slot/4-pole PMSM
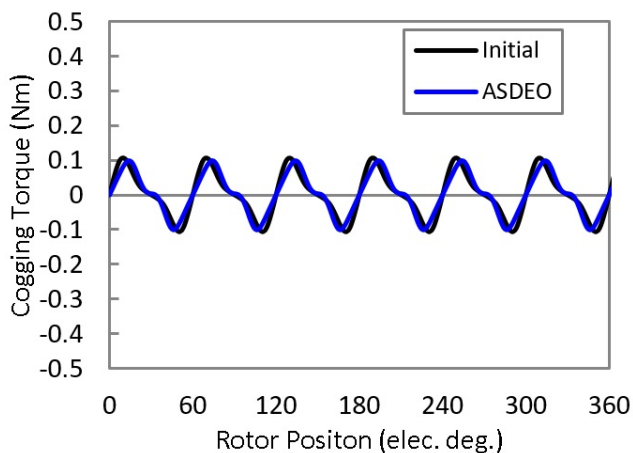
as shown in Figure 7. Table 4 shows the magnitudes of each harmonic component in the phase back-emf waveform. The total harmonic distortion is reduced to 4.2 % after the motor has been optimized.

Cogging torque

Generally, the cogging torque exists due to the interaction between the stator slots and magnetic pole edges resulting in unwanted torque ripples, noise and vibration. Therefore, it is always desirable to design PMSM with negligible cogging torque. The motor models in 2D FEM have been used to compute the cogging torque waveform in 6-slot/4-pole motor, and their results are shown in Figure 8. The smallest common multiple N_{scm} for 6-slot/4-pole motor is 12[15,16]. Usually higher N_{scm} will result in smaller cogging torque[15]. The cogging torque waveform is repeating every 60^0 electrical. Its peak is about 0.1 Nm.

Output Torque

The output torque during on-load condition is simulated in 2D FEM rotating machine analysis by subjecting the motor to sinusoidal current excitation of 5 A peak. The average output torque has increased to
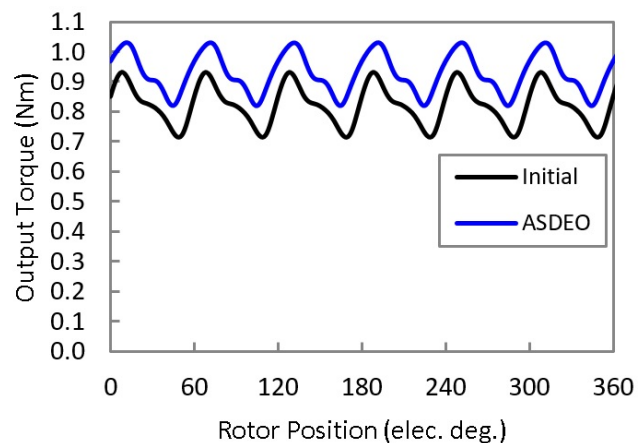
0.928 Nm but it has nearly similar torque ripple before and after optimization as shown in Figure 9 and Table 5. This is due to the effects of cogging torque and also THDv contents in back-emf waveform. However, this output torque ripple can be further minimized by applying the cogging torque reduction technique[23,25].

Conclusion

The performance of three-phase, 6-slot/4-pole permanent magnet synchronous motor (PMSM) has been enhanced by using analytical sub-domain model integrated with differential evolution optimization (ASDEO). Five motor parameters were optimized, i.e., magnet pole arc, magnet thickness, air gap length, slot opening, and stator inner radius. Four objective functions were selected, i.e., to have high efficiency, high output torque, low cogging torque, and low total harmonic distortion in phase back-emf. The Pareto chart is used to tabulate the potential motor performance for certain optimized motor parameters, providing the freedom to choose the suitable motor performance value. The optimized 6-slot/4-pole motor has high efficiency and high fundamental phase

back-emf. Consequently, the average output torque of the motor has been improved. The results from 2D FEM confirms the motor performance accuracy from ASDEO in designing the three-phase PMSM for underwater propulsion system.

Acknowledgement

References
1 Balamurugan Nachimuthu, and Selvaperumal Sundramoorthy, Intelligent controller for speed control of three phase induction motor using indirect vector control method in marine applications, *Indian J. Geo-Mar. Sci.*, 47(05), (2018), 1069-1074.
2 Selvaperumal, S., Nedumal Pugazhenthi, P., Amudha, A., Closed loop performance investigation of various controllers based chopper fed DC drive in marine applications, *Indian J. Geo-Mar. Sci.*, 46(05), (2017), 1044-1051.
3 Muthulakshmi, S. and Dhanasekaran, R. A new switched reluctance motor drive using passive network for marine propulsion, *Indian J. Geo-Mar. Sci.*, 44(11), (2015), 1807-1814.
4 Mohd-Mokhtar, R., Aziz, M.H.R.A., Arshad, M.R., Husaini, A.B., Noh, M.M. Model identification and control analysis for underwater thruster system, *Indian J. Geo-Mar. Sci.*, 42(8), (2013), 992-998.
5 Mohd Akmal Mohd Yusoff, Mohd Rizal Arshad, Muzammer Zakaria, Diagnosis of thruster fault condition using statistical design of experiment, *Indian J. Geo-Mar. Sci.*, 41(6), (2012), 550-556.
6 Muljowidodo, K., Sapto Adi, N., Nico Prayoga, Agus Budiyono, Design and testing of underwater thruster for SHRIMP ROV-ITB, *Indian J. Mar. Sci.*, 38(3), (2009), 338-345.
7 Ishak, D., Manap, N.A.A., Ahmad, M.S. and Arshad, M.R. Electrically actuated thrusters for autonomous underwater vehicle, *11th IEEE International Workshop on Advanced Motion Control (AMC)*, Nagaoka, Niigata, 2010, pp. 619-624.
8 Choi, J.S., and Yoo, J., Optimal design method for magnetization directions of a permanent magnet array, *J. Magn.Magn. Mater*, 322(15), (2010), 2145-2151.
9 Rahideh, A., and Korakianitis, T., Analytical magnetic field calculation of slotted brushless permanent-magnet machines with surface inset magnets, *IEEE Trans. Magn.*, 48(10), (2012), 2633-2649.
10 Miyamasu, M., and Akatsu, K., A study of high torque surface-mounted permanent magnet synchronous motor by maximum utilization of the magnet flux, *15th International Conference on Electrical Machines and Systems (ICEMS)*, Sapporo, Japan, 2012, pp. 1-6.
11 Pfister, P.D., and Perriard, Y., Slotless permanent-magnet machines: general analytical magnetic field calculation, *IEEE Trans. Magn.*, 47(6), (2011), 1739-1752.

12 Atallah, K., Zhu, Z.Q. and Howe, D., Armature reaction field and winding inductances of slotless permanent-magnet brushless machines, *IEEE Trans. Magn.*, 34(5), (1998), 3737-3744.
13 Rahideh, A., and Korakianitis, T., Analytical calculation of open-circuit magnetic field distribution of slotless brushless PM machines, *Int. J. Electr. Power Energy Syst.*, 44(1), (2013), 99-114.
14 Stjepan Stipetic, Werner Miebach, and Damir Zarko, "Optimization in Design of Electric Machines: Methodology and Workflow," in ACEMP - OPTIM - ELECTROMOTION joint conference, 2015. http://www.adept-itn.eu/images/ Publications/Optimization_in_Design_of_Electric_Machines_ Methodology_and_Workflow.pdf. [Online: 24 March 2016]
15 Ahmad, M.S., Manap, N.A.A. and Ishak, D., Permanent magnet brushless machines with minimum difference in slot number and pole number, *2nd International Conference on Power and Energy 2008 (PECON)*, Johor Bharu, Malaysia, 2008, pp. 1064-1069.
16 Zhu, Z.Q., Ruangsinchaiwanich, S., Ishak, D. and Howe, D., Analysis of cogging torque in brushless Machines having nonuniformly distributed stator slots and stepped rotor magnets, *IEEE Trans. Magn.*, 41(10), (2005), 3910-3912.
17 Lubin, T., Mezani, S. and Rezzoug, A. 2-D exact analytical model for surface-mounted permanent-magnet motors with semi-closed slots, *IEEE Trans. Magn.*, 47(2), (2011), 479-492.
18 Wu, L.J., Zhu, Z.Q., Staton, D., Popescu, M. and Hawkins, D. An improved subdomain model for predicting magnetic of surface-mounted permanent magnet machines accounting for tooth-tips, *IEEE Trans. Magn.*, 47(6), (2011), 1693-1704.
19 Gilson, A., Tavernier, S., Dubas, F., Depernet, D. and Espanet, C. 2-D analytical subdomain model for high-speed permanent-magnet machines, *18th International Conference on Electrical Machines and Systems (ICEMS)*, Pattaya, 2015, pp. 1508-1514.
20 Tiang, T.L., Ishak, D., Lim, C.P., Jamil, M.K.M. A comprehensive analytical subdomain model and its field solutions for surface-mounted permanent magnet machines, *IEEE Trans. Magn.*, 51(4), (2015), 1-14.
21 Abazar Shamekhi, An Improved Differential Evolution Optimization Algorithm, *Int. J. Res. & Rev. Appl. Sci.*, 15(2), (2013), 132-145.
22 Mumtaz Muetler and Osman Bilgin, Comparison of stochastic optimization methods for design optimization of permanent magnet synchronous motor, *Neural Computing and Applications*, 21(8), (2012), 2049-2056.
23 Goga Cvetkovski, Lidija Petrovska, and Paul Lefley, Topological modifications in function of cogging torque reduction of permanent magnet synchronous motor, *Przeglad Electrotechniczny*, 2014(12), (2014), 113-115.
24 Melcescu, L., Covrig, M. and Moraru, A. Analyses of core skewing influence in permanent magnet synchronous machine by 2D FEM field computation, *U. P. B. Sci. Bull. Series C*, 68(2), (2006), 41-52.
25 Kudrjavtsev, O. and Kilk, A. Cogging torque reduction methods, *Electrical Power Quality Supply Reliability Conference*, 2014, pp. 251-254.